Molecular Therapy
Nucleic Acids
Original Article

Anti-tumor Activity of miniPEG-γ-Modified PNAs to Inhibit MicroRNA-210 for Cancer Therapy

Anisha Gupta,[1] Elias Quijano,[2] Yanfeng Liu,[1] Raman Bahal,[3] Susan E. Scanlon,[1] Eric Song,[2] Wei-Che Hsieh,[4] Demetrios E. Braddock,[5] Danith H. Ly,[4] W. Mark Saltzman,[2] and Peter M. Glazer[1,6]

[1]Department of Therapeutic Radiology, Yale University, New Haven, CT 06510, USA; [2]Department of Biomedical Engineering, Yale University, New Haven, CT 06520, USA; [3]Department of Pharmaceutical Sciences, University of Connecticut, Storrs, CT 06269, USA; [4]Department of Chemistry and Center for Nucleic Acids Science and Technology (CNAST), Carnegie Mellon University, Pittsburgh, PA 15213, USA; [5]Department of Pathology, Yale University, New Haven, CT 06510, USA; [6]Department of Genetics, Yale University, New Haven, CT 06510, USA

MicroRNAs (miRs) are frequently overexpressed in human cancers. In particular, miR-210 is induced in hypoxic cells and acts to orchestrate the adaptation of tumor cells to hypoxia. Silencing oncogenic miRs such as miR-210 may therefore offer a promising approach to anticancer therapy. We have developed a miR-210 inhibition strategy based on a new class of conformationally preorganized antisense γ peptide nucleic acids (γPNAs) that possess vastly superior RNA-binding affinity, improved solubility, and favorable biocompatibility. For cellular delivery, we encapsulated the γPNAs in poly(lactic-co-glycolic acid) (PLGA) nanoparticles (NPs). Our results show that γPNAs targeting miR-210 cause significant delay in growth of a human tumor xenograft in mice compared to conventional PNAs. Further, histopathological analyses show considerable necrosis, fibrosis, and reduced cell proliferation in γPNA-treated tumors compared to controls. Overall, our work provides a chemical framework for a novel anti-miR therapeutic approach using γPNAs that should facilitate rational design of agents to potently inhibit oncogenic microRNAs.

INTRODUCTION

MicroRNAs (miRs) are small RNA molecules that regulate gene expression at the post-transcriptional level.[1,2] miRs frequently show differential expression in cancer and affect cellular transformation, carcinogenesis, and metastasis by acting either as oncogenes (so-called oncomiRs) or tumor suppressors.[3–6] In response to hypoxia, which typically occurs during progression of tumors, various oncomiRs are significantly upregulated.[7,8] In particular, miR-210 is upregulated in response to hypoxia in various cancer cells.[9–11] Furthermore, high levels of miR-210 have been detected in almost all solid tumors examined, including breast, cervical, pancreatic, and colorectal cancer.[11,12] In addition, a significant increase of circulating miR-210 has been found in the serum of patients with various malignancies, including lymphoma,[13] pancreatic cancer,[10] and renal cell carcinoma.[14] A number of miR-210 targets have been identified, pointing to its roles in DNA repair,[9] mitochondrial oxidative metabolism,[15] and cell survival[16] and broadly in the cellular adaptation to hypoxia.[17] Taken together, these studies suggest that miR-210 may play a key role in the ability of tumor cells to survive and proliferate under hypoxic conditions. We therefore hypothesized that miR-210 might be an effective target for anti-cancer therapy. To test our hypothesis, we sought to develop molecules that can potently antagonize the activity of miR-210.

To inhibit miRs, a promising strategy is the use of antisense oligonucleotides, referred to as anti-miRs. They are designed to bind by Watson-Crick complementarity to the mature miRs and thereby prevent interaction with target mRNAs.[18–21] Current molecular approaches for the design of anti-miRs are centered on chemically modified RNA-based oligonucleotides, notably locked nucleic acids (LNAs),[22,23] 2′-O-methyl oligonucleotides, and peptide nucleic acids (PNAs).[24–27] PNAs are synthetic DNA mimics, in which the phosphodiester backbone is substituted with a charge-neutral *N*-(2-aminoethyl) glycine backbone (Figure 1A).[28] PNAs hybridize to single-stranded nucleic acid targets by Watson-Crick base pairing with high binding affinities compared to other nucleic acid analogs[28] and are not susceptible to degradation by proteases or nucleases. It has been shown that an anti-miR PNA encapsulated in poly(lactide-co-glycolide) (PLGA) nanoparticles (NPs) can inhibit the expression of a lymphoma-associated oncomiR, miR-155, in vivo in mice.[29] We have recently shown anti-tumor effects via delivery of an anti-miR-155 PNA to tumors by conjugation to a pH low insertion peptide (pHLIP).[21] However, regular unmodified PNAs have certain limitations as a therapeutic agent, including low solubility in aqueous solution and a tendency to aggregate. To overcome these limitations, our group has developed a chemically modified version of PNA substituted at the γ position. γPNAs are conformationally pre-organized into a right-handed helical motif due to the (*R*)-stereogenic center at the γ-backbone through which the hydrophilic (diethylene glycol) moiety is attached (also called miniPEG-γPNA or ^{MP}γPNA) (Figure 1A). ^{MP}γPNAs possess superior properties, including high water solubility, increased binding affinity for RNA and DNA, and improved biocompatibility.[30,31] We have shown that ^{MP}γPNAs can

Received 28 January 2017; accepted 6 September 2017;
https://doi.org/10.1016/j.omtn.2017.09.001.

Correspondence: Peter M. Glazer, Department of Therapeutic Radiology, Yale University, New Haven, CT 06510, USA.
E-mail: peter.glazer@yale.edu

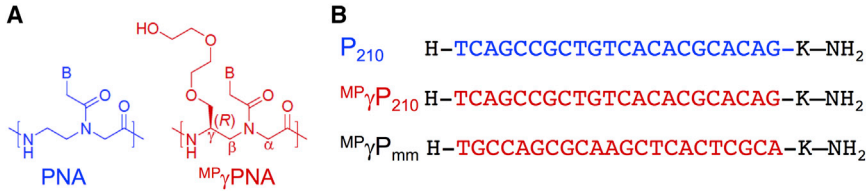

Figure 1. PNA Structure and Sequences

(A) Chemical structure of regular PNA and a gamma PNA containing mini-PEG residue at the gamma carbon. (B) PNA oligomers designed to target miR-210: regular PNA (P_{210}), gamma PNA ($^{MP}\gamma P_{210}$), and the control mismatched gamma PNA ($^{MP}\gamma P_{mm}$). Red indicates the gamma (γ) modifications. The PNA sequences are written from N to C termini. K stands for lysine.

be used as antisense agents to target mRNAs[32] and as triplex-forming molecules for stimulating gene editing.[33] On the basis of the advantageous properties of $^{MP}\gamma$PNAs, we hypothesized that they might also show superior activity for antagonizing miR-210 in comparison to regular PNAs. To test our hypothesis, we designed a miR-210 inhibition strategy based on $^{MP}\gamma$PNA. We find that $^{MP}\gamma$PNAs designed to inhibit miR-210 and be delivered via PLGA NPs show substantially more potent suppression of tumor growth when compared to regular PNAs in human tumor xenografts. We also show that the $^{MP}\gamma$PNA induces marked apoptosis and necrosis within treated tumors. These results highlight the superiority of $^{MP}\gamma$PNA as an anti-miR agent, with better miR-210 inhibition and anti-tumor efficacy compared to that of classic PNA molecules.

RESULTS

Design and Characterization of Anti-miR-210 γPNAs

To target miR-210, we designed a 22-nt PNA sequence to be complementary to the mature miR-210-3p, which is upregulated in response to hypoxia (Figure 1B). P_{210} comprises regular PNA units, whereas $^{MP}\gamma P_{210}$ has the same sequence as P_{210} but is fully substituted with $^{MP}\gamma$PNA building blocks. As a control, we also synthesized a mismatched γPNA ($^{MP}\gamma P_{mm}$), consisting of all $^{MP}\gamma$PNA units but with a mismatched sequence compared to that of $^{MP}\gamma P_{210}$. Based on prior work, the chiral $^{MP}\gamma$ substitution is expected to enforce a pre-organized helical conformation.[31,34] We used circular dichroism analyses to interrogate the secondary structure of the PNAs and confirm the pre-organization in $^{MP}\gamma$PNAs (Figure S1A). We found that $^{MP}\gamma P_{210}$ and $^{MP}\gamma P_{mm}$ showed distinct exciton coupling patterns, with minima at λ 242 nm and λ 280 nm and maxima at λ 260 nm, characteristic of a right-handed helix.[35] In contrast, P_{210} did not show any of these characteristic CD signatures. These results confirm the predicted, preorganized helical motif of γPNAs. To assess the binding capability of PNAs to miR-210, we performed electrophoretic mobility shift assays. RNA corresponding to the 22-nt mature miR-210 target sequence was synthesized and incubated with increasing concentrations of P_{210} and $^{MP}\gamma P_{210}$ at a physiological temperature. Shifted bands were observed in both cases, representing the formation of heteroduplexes (Figure S1B). As shown in Figure S1B, upon increasing the concentration of P_{210}, we observe that the intensity of the shifted band gets decreased. Due to a higher concentration, it might bind with a strong binding affinity, which could preclude SybrGold to bind the complex. This is even more apparent in the case of γP210, which binds with the RNA with a strong binding affinity, possibly leading to a weaker signal of the shifted band due to a decreased ability of the SybrGold to bind.

Further, we performed UV melting experiments to determine the thermal stability of the PNAs upon hybridization to RNA and DNA containing the 22-nt mature miR-210 target sequence. The perfectly matched $^{MP}\gamma P_{210}$ exhibited high thermal stability (>90°C) to both RNA (Figure S2A) and DNA (Figure S2B), even under denaturing conditions of 5M urea. Without the backbone preorganization, achiral regular PNA, P_{210} had lower thermal stability upon hybridization to RNA (81°C) and DNA (76°C). The backbone preorganization also enhanced sequence discrimination capability because the mismatched sequence duplexes ($^{MP}\gamma P_{mm}$-RNA and $^{MP}\gamma P_{mm}$-DNA) had significantly lowered thermal stabilities (45°C). The formation of PNA-RNA and PNA-DNA duplexes in the case of $^{MP}\gamma P_{210}$ (which does not show a clear melting transition) was further confirmed by CD spectra (Figures S2C and S2D). Both P_{210} and $^{MP}\gamma P_{210}$ showed typical antiparallel heteroduplex CD spectra, with a maximum at 262 nm and negative minima at 240 and 287 nm. In addition, the mismatched duplexes ($^{MP}\gamma P_{mm}$-RNA and $^{MP}\gamma P_{mm}$-DNA) did not induce a CD intensity compared to that of the perfectly matched duplexes, confirming the sequence discrimination data obtained from the UV-melting experiments.

NP Formulation and Characterization

To deliver PNAs in vivo, we formulated P_{210} and $^{MP}\gamma P_{210}$ into PLGA NPs by a double-emulsion solvent evaporation technique.[36] We also prepared blank NPs containing no PNA and NPs containing $^{MP}\gamma P_{mm}$ as controls. All three NP batches show uniform morphologies by scanning electron microscopy (Figure 2A). All batches consisted of NPs in the diameter range of 200–300 nm, as measured by dynamic light scattering (Table 1), consistent with previously published measurements of NPs formulated with standard PNA cargoes or with combinations of PNA and DNA oligomers.[32,37] PNA-loaded NPs showed a small negative surface charge, also expected for PLGA NPs (Table 1). The kinetics of PNA released from NPs was measured by incubation in buffered saline; both γPNAs ($^{MP}\gamma P_{210}$ and $^{MP}\gamma P_{mm}$) were released from the NPs more rapidly than the regular PNA (P_{210}), with 60%–70% of γPNAs released within 8 hr versus 25% of P_{210} (Figure 2B). The more rapid release of the γPNAs is likely due to their more hydrophilic nature. The average loading of PNA was ~150 pmol/mg of NP. PNA-containing NPs rapidly enter HeLa cells, a human cervical carcinoma cell line, in culture after the addition of NPs to the culture medium (Figure 2C).

miR-210 Is Upregulated in HeLa Tumors

In prior work, we have found that hypoxic conditions upregulate miR-210 in HeLa and MCF7 cell lines,[9] so we chose HeLa cells as a

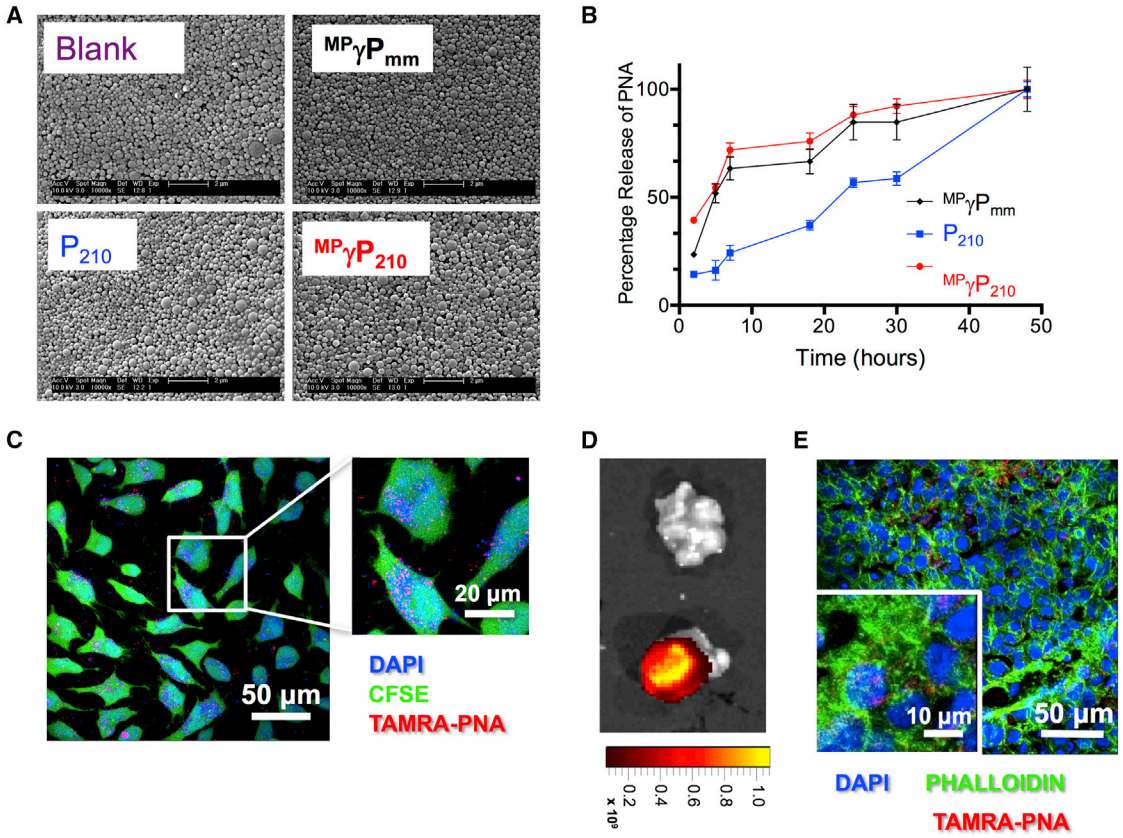

Figure 2. Nanoparticle Characterization and PNA Uptake

(A) Scanning electron microscopy images showing uniform morphology of nanoparticles. Scale bar, 2 μm. (B) PNA release profiles of PNAs from the nanoparticles (n = 3, data represented as mean ± SE). (C) z stacked confocal microscopy images showing uptake of TAMRA-labeled PNA (red) in live HeLa cells in culture after incubation for 24 hr. Free intracellular amines and nuclei were stained with CFSE (green) and DAPI (blue), respectively, to visualize PNA location relative to different cellular compartments. Scale bars, 20 μm and 50 μm, as indicated. (D) Localization of a TAMRA-conjugated PNA in HeLa tumors. A tumor treated with TAMRA-conjugated PNA-containing nanoparticles (bottom) showed localization of PNA in the tumor in comparison to the tumor treated with blank nanoparticles. These images were acquired using the IVIS Spectrum System (Caliper). (E) Confocal images showing uptake of TAMRA-labeled PNA (red) within tumor cells after tumors in (D) were cryosectioned and stained. Scale bars, 10 μm and 50 μm, as indicated. Actin and nuclei were stained with Phalloidin (green) and DAPI (blue), respectively.

tumor model. We analyzed the miR-210 expression levels in HeLa tumors (grown as xenografts in immune-deficient nude mice) in comparison with miR-210 levels in cells grown in culture under normoxia or transient hypoxia (0.5% O_2 for 24 or 48 hr). Although miR-210 was induced in the hypoxic HeLa cells in culture, as observed in prior work,[9] it is worth noting that the levels of miR-210 expression in the HeLa cells derived from the tumors were substantially higher. To evaluate miR-210 levels in the HeLa cell component within the tumor, we enzymatically dissociated cells within the tumors and immune depleted the murine cells. We found that miR-210 levels in the HeLa cells within the tumors were 1.5- to 2.5-fold higher than the levels seen in HeLa cells grown under hypoxic condition culture and more than 25-fold above the normoxic cells (Figure 3A). These findings suggest that adaptation of cancer cells to growth in the complex tumor microenvironment, characterized by abnormal vasculature, fluctuating acute and chronic hypoxia, acidosis, and transient nutrient deprivation, may require even higher levels of miR-210 than those just observed after transient hypoxia exposure of cells in culture. Further, we compared the miR-210 levels in tumor HeLa cells versus the overall levels in the bulk tumor, which includes murine vasculature and other mouse stromal cells. Interestingly, we found higher expression of miR-210 in the bulk tumor than in the tumor HeLa cells by themselves, indicating that the mouse stromal cells in the tumor also express high levels of miR-210. We hypothesized that these highly elevated levels of miR-210 might play a vital role in tumor survival, providing the context for testing the effectiveness of anti-miR-210 PNAs.

NPs Carrying Anti-miR-210 γPNAs Substantially Reduce Tumor Growth

Given the high levels of miR-210 expression in HeLa tumors, we tested the impact on tumor growth upon treatment with NPs containing the anti-miR-210 PNAs, either P_{210} or $^{MP}\gamma P_{210}$, in comparison to blank NPs or NPs containing the mismatched sequence

Table 1. Charge Potential and Size Analysis of the Nanoparticles

NP	Zeta Potential (mV)	Diameter (nm)
Blank	−19.0 ± 0.6	290 ± 5.1
$^{MP}\gamma P_{mm}$	−23.5 ± 0.2	320 ± 1.8
P_{210}	−28.0 ± 0.5	390 ± 6.9
$^{MP}\gamma P_{210}$	−23.5 ± 0.3	310 ± 5.0

PNA $^{MP}\gamma P_{mm}$ (Figure S3A). To assess the distribution of PNA after treatment, NPs were administered by intratumoral injection and localization of 5-carboxytetramethylrhodamine (TAMRA)-labeled PNA in the tumors was assayed 24 hr later by in vivo imaging system (IVIS) imaging of the gross tumor samples and confocal microscopy of tumor sections (Figures 2D and 2E), confirming distribution of the PNAs within the tumor cells. For tumor growth delay assays, tumors were injected locally with 6 mg of NPs and tumor growth was measured three times per week (Figure S3A). We found that the NPs containing $^{MP}\gamma P_{210}$ significantly diminished the tumor growth over the course of the experiment compared to all the other NPs, even the NPs containing the regular but still targeted PNA P_{210} (Figure 3B). By day 36, blank, P_{210}-, and $^{MP}\gamma P_{mm}$-treated tumors all showed an average increase in tumor volume of 6-fold, whereas the $^{MP}\gamma P_{210}$-treated tumors showed an approximately 3-fold increase at that time point. A Kaplan-Meier plot with a survival endpoint of 3x tumor growth in size relative to the pre-treatment volume shows significantly longer survival in the $^{MP}\gamma P_{210}$-treated group as compared to the other groups (Figure 3C). On the day mice were sacrificed, tumors were photographed to document gross morphology (Figure 3D). Notably, tumors treated with $^{MP}\gamma P_{210}$-loaded NPs were smaller, showing rounder tumor morphology, and were softer to palpation in comparison to the more irregular appearance and harder consistency of the tumors treated with the other NPs (Figure 3D).

The tumor growth delay experiment was repeated using naked PNAs without NP formulation. We found that the naked $^{MP}\gamma P_{210}$-treated group showed some effect on tumor growth suppressions, but it was not statistically significant when compared to the corresponding naked PNA controls (Figure S4A), in contrast to the statistically significant tumor growth suppression mediated by the NP formulation of the same molecule. In addition, we found that intravenous administration of the NPs via retro-orbital injection was not effective in delaying tumor growth (Figure S4B); we suspect that surface modification of the particles may be needed to enhance tumor accumulation of the NPs.[38]

Effect of PNA Treatment on miR-210 Levels and on Expression of a Known miR-210 Target, ISCU, in the Tumors

To correlate with the differential effect on tumor growth, we compared miR-210 expression levels by RT-PCR in RNA isolated from the HeLa tumor cells in $^{MP}\gamma P_{210}$-treated tumors versus HeLa cells from tumors treated with $^{MP}\gamma P_{mm}$. The $^{MP}\gamma P_{210}$-treated tumors showed a more than 2-fold decrease in miR-210 levels compared to those of the $^{MP}\gamma P_{mm}$-treated tumors (Figure 3E). To determine whether the γPNAs might also affect murine miR-210 levels, we also evaluated miR-210 levels in mouse cells saved after using a mouse cell depletion kit on treated tumors. As shown in Figure S4, we also observed a reduction in miR-210 expression levels in RNA obtained from the murine stromal cells from $^{MP}\gamma P_{210}$-treated tumors (Figure S5).

A predicted effect of inhibition of miR-210 would be the rescue in expression of ISCU protein, a known downstream target of miR-210 that has been shown to be suppressed upon increased expression of miR-210 under hypoxic conditions.[15,39] To confirm miR-210 inhibition at a functional level in the tumors treated with $^{MP}\gamma P_{210}$, we compared ISCU protein levels in the HeLa tumor cells derived from the $^{MP}\gamma P_{210}$-treated tumors with those from $^{MP}\gamma P_{mm}$-treated tumors. $^{MP}\gamma P_{210}$-treated tumors showed a higher expression of ISCU (Figure 3F). These results are consistent with in vivo inhibition of miR-210 activity at the molecular level by the NPs containing $^{MP}\gamma P_{210}$.

Histopathologic Analyses of $^{MP}\gamma P_{210}$-Treated Tumors

We performed histopathological analyses to correlate with the therapeutic response, as measured by tumor growth delay (Figure S3B). Histopathological analyses showed regions of central coagulative necrosis in the $^{MP}\gamma P_{210}$-treated tumors (Figure 4A), whereas blank, P_{210}-, and $^{MP}\gamma P_{mm}$-treated tumors showed a viable tumor without substantial necrosis. Also, $^{MP}\gamma P_{210}$-treated tumors showed dense fibrosis based on trichrome staining (Figure 4A). This induced fibrosis could be due to a combined effect of reduced miR-210 levels in the tumor cells and in the murine vasculature and stroma. Caspase staining was also performed as a marker of apoptosis, and this revealed higher levels of apoptosis in the $^{MP}\gamma P_{210}$-treated tumors compared to the others (Figure 4B). In addition, the effect of PNA treatments on cell proliferation was interrogated by Ki-67 staining, which is a specific biomarker of proliferating cells. $^{MP}\gamma P_{210}$-treated tumors showed the fewest positive Ki-67 cells (Figure 4B).

DISCUSSION

Here, we report that chemically modified $^{MP}\gamma$PNAs, designed to inhibit a tumor-associated microRNA, miR-210, can mediate effective suppression of tumor growth when delivered via PLGA NPs. Importantly, the $^{MP}\gamma P_{210}$ NPs showed much greater suppression of tumor growth compared to the effect of NPs containing regular PNA of the same sequence (P_{210}). Possible explanations for this difference include the greater binding affinity conferred by the γ modification and the favorable release profile exhibited by γPNAs from the PLGA particles. In reference to prior work, anti-miRs consisting of regular PNAs targeting miR-155 in a mouse lymphoma model showed substantial in vivo activity in two sets of experiments, but in both cases, the delivery methods were enhanced. In one case, the PNAs were carried in PLGA NPs that were coated with a cell-penetrating peptide to improve cellular uptake.[38] In the other, the PNAs were delivered by conjugation to a pHLIP capable of robust transmembrane insertion in the acidic tumor microenvironment.[21]

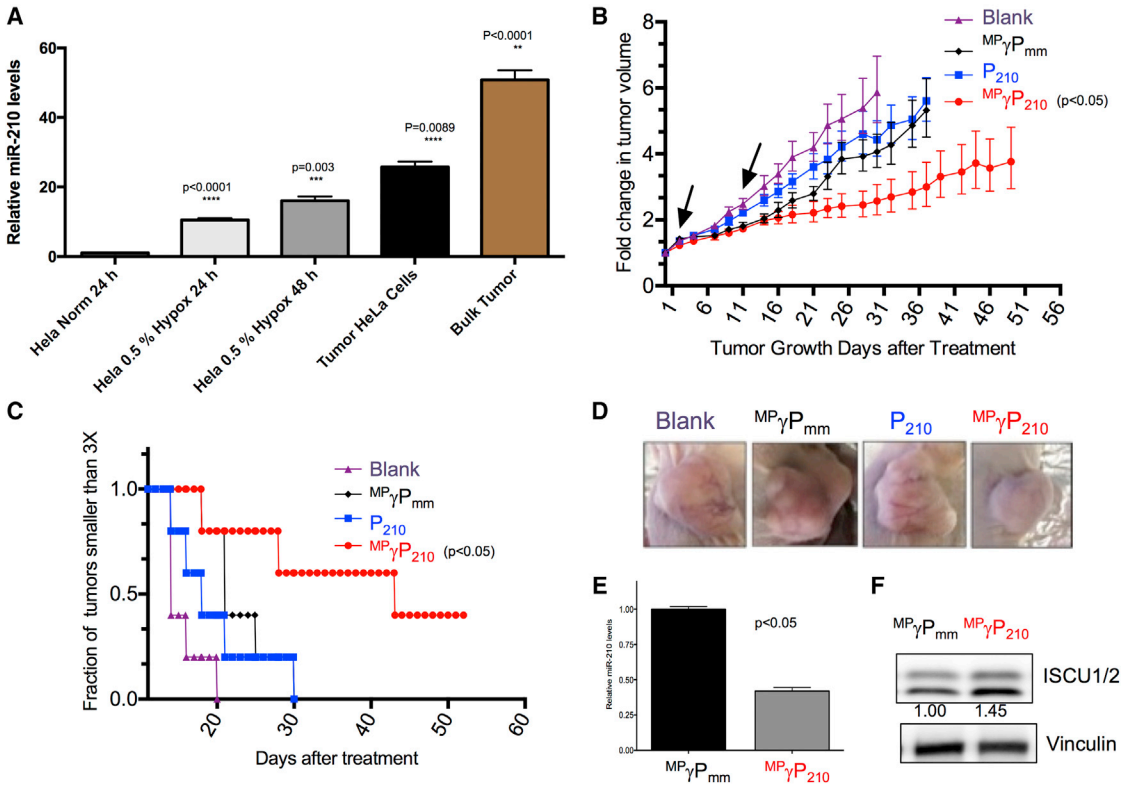

Figure 3. Effect of PNA-Loaded NPs In Vivo

(A) miR-210 overexpression in isolated HeLa tumor cells and in the bulk tumors from xenograft mouse models compared to HeLa cells incubated for 24 or 48 hr in 0.5% hypoxia (n = 3, data represented as mean ± SE). t test was used for statistical analysis relative to normoxic HeLa cells. (B) Fold-change in tumor growth in response to locally administered anti-miRs. Arrowhead represents 6-mg nanoparticle injection (n = 5 for each group, data represented as mean ± SEM). ANOVA was used for statistical analysis for each group relative to the blank group. (C) Number of days for tumors to reach 3x their initial volume at the time of treatment (n = 5 for each group, data represented as mean ± SEM). Long-rank test was used for statistical analysis for each group relative to the blank group. (D) Representative tumor images after intratumoral treatment of nanoparticles. In accordance with animal care regulations, mice were euthanized after tumors reached a volume of 1,000 mm^3 for the control blank, mismatched γPNA, and regular PNA-treated group. Because the gamma PNA-treated mice showed a delayed tumor growth, they were maintained for a longer period and euthanized 46 days after treatment. The tumor images were taken before the mice were euthanized. (E) Relative miR-210 levels in RNA extracted from HeLa tumor cells derived from xenograft tumors treated with the indicated nanoparticles (n = 3, data represented as mean ± SE). t test was used for statistical analysis, $p < 0.05$. (F) Western blot of protein extracted from tumors treated with the indicated nanoparticles.

In contrast, our current results demonstrate that ^{MP}γPNAs can effectively inhibit an oncogenic microRNA, even when delivered by simple PLGA NPs without any specialized modifications or specialized peptide conjugates. However, we expect that the superior activity of the γPNAs will be further augmented by other delivery methods, which will be the subject of future work. A prior report has shown an anti-miR-155 effect at a dose of 1.5 mg/kg via local treatment of PNA contained within PLGA NPs coated with a cell-penetrating peptide.[38] Our γPNA shows an anti-miR-210 effect at a dose of 0.8 mg/kg via local treatment of unmodified PLGA NPs.

Notably, in recent studies investigating triplex-forming PNAs for gene editing, we found that γPNAs showed 3- to 5-fold increases in activity compared to regular PNAs,[37] even with only partial substitution at alternating residues. In that gene editing work, the PNAs were combined with donor DNAs and encapsulated in PLGA NPs, which were injected intravenously into thalassemic mice, with the goal of correcting a point mutation in the β-globin gene. Treatment of the mice with NPs containing triplex-forming γPNAs yielded sufficient gene editing in bone marrow stem cells to mediate complete correction of the anemia in the mice. Taken together, our current studies and the gene-editing results provide strong support to pursue continued development of γPNAs. In this regard, it is possible to incorporate other side chains besides miniPEG[40,41] and to substitute non-natural nucleobases that may have advantages, as have been described.[42]

With regard to the miR-210 target, studies have reported conflicting roles for miR-210 in tumorigenenesis. A number of publications point to the oncogenic potential of miR-210 in head and neck squamous cell carcinoma,[43] breast cancer,[44] and hepatomas.[45,46] On the other hand, one study using engineered cell lines suggested that ectopic miR-210 overexpression can suppress the rate of tumor initiation in immune-deficient mice, although once formed, tumor

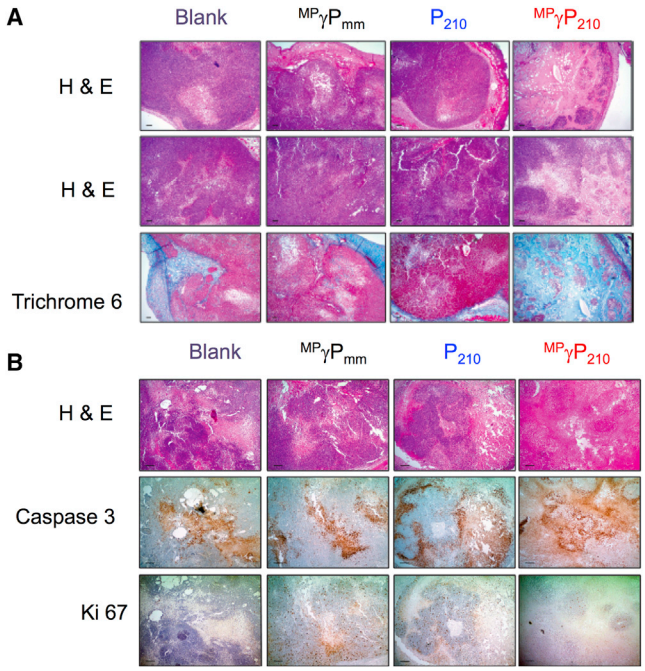

Figure 4. Histopathologic Analysis of Treated Tumors

Tumors were ranked according to intratumoral necrosis from most to least in a blinded fashion, and representative sections from each treatment group are shown in the figure. (A) Two H&E sections representative of tumors in each treatment group are shown, with a trichrome stain to highlight fibrosis. Only capular fibrosis is present in each treatment group, with the exception of $^{MP}\gamma P_{210}$, which showed intratumoral necrosis (H&E) and dense intratumoral fibrosis (Trichrome 6) in some animals, consistent with tumor regression immediately following treatment. Mice were sacrificed on day 3 after treating with 6 mg nanoparticles. Scale bars represent 5 μm. (B) Photomicrographs of representative tumors and corresponding special stains to highlight apoptosis and proliferative index. H&E examination demonstrated areas of tumor necrosis in all treatment groups, but was most pronounced in the $^{MP}\gamma P_{210}$ treatment group. The tumor necrosis present is due to apoptosis, as demonstrated by caspase-3 staining. The proliferative index of all treatment groups is low and comparable in the viable tumor cells (1 out of 4 or about 10%–15% of total tumor cells), but due to the extensive necrosis in the $^{MP}\gamma P_{210}$ treatment group, the overall proliferative index of the tumor $^{MP}\gamma P_{210}$ is reduced (less than 2% to 3%). Mice were sacrificed on day 3 after treating with 6-mg nanoparticles. Scale bars represent 5 μm.

growth proceeded normally.[47] In another, deletion of the locus expressing miR-210 was reported in some human ovarian carcinomas.[48] Nonetheless, our findings suggest that inhibiting miR-210 via anti-miR PNAs can suppress tumor growth in vivo. Besides tumor growth suppression, we found immunohistochemical evidence for increased apoptosis, necrosis, and fibrosis and decreased cell proliferation induced by $^{MP}\gamma P_{210}$ compared with the regular PNA and with the blank and mismatched controls. These results are fully in keeping with findings by Yang et al.,[46] who observed that lentivirus-mediated knockdown of miR-210 inhibited proliferation and apoptosis in a human hepatoma xenograft. Further, they found that lentivirus knockdown of miR-210 synergized with ionizing radiation in suppressing tumor growth,[46] raising the additional possibility that $^{MP}\gamma$PNA anti-miR therapy directed at miR-210 may eventually prove valuable in combination with chemotherapy or radiotherapy.

In summary, our studies demonstrate that the modified γPNA delivered via polymeric NPs antagonizes the expression of miR-210 in a HeLa cancer model, resulting in an anticancer effect with no observed toxicities. These findings provide a means for cancer therapy by effective targeting of miRNA.

MATERIALS AND METHODS

PNA Monomer Synthesis

Regular Boc-protected PNA monomers were purchased from ASM Research Chemicals. MiniPEG-γPNA monomers were synthesized using Boc-protected L-serine as a starting material, as previously reported by Sahu and coworkers.[49]

PNA Synthesis

All oligomers were synthesized on solid support using standard Boc chemistry procedures. The oligomers were cleaved from the resin using an m-cresol:thioanisole:trifluoromethanesulfonic acid (TFMSA):trifluoroacetic acid (TFA) (1:1:2:6) cocktail solution. The resulting mixtures were precipitated with ether, purified, and characterized by reverse phase–high performance liquid chromatography (RP-HPLC) and MALDI-TOF, respectively. All PNA stock solutions were prepared using nanopure water, and the concentrations were determined at 90°C on a Cary 3 Biospectrophotometer using the following extinction coefficients: 13,700 $M^{-1}cm^{-1}$ (A), 6,600 $M^{-1}cm^{-1}$ (C), 11,700 $M^{-1}cm^{-1}$ (G), and 8,600 $M^{-1}cm^{-1}$ (T).

Circular Dichroism Analyses

CD samples were prepared at 5 μM strand concentrations in sodium phosphate buffer (10 mM sodium phosphate, 100 mM NaCl, 0.1 mM EDTA, and 5 M urea) at pH 7. The samples were heated to 95°C and gradually cooled down to room temperature. CD experiments were performed on a JASCO J-715 spectropolarimeter using a quartz cuvette with 1-cm path length. The samples were scanned from 320 to 200 nm with a scan rate of 100 nm/min and 15 scan accumulation at 25°C. All spectra were processed using Origin software, and baseline was subtracted and, unless otherwise noted, smoothed using a five-point adjacent averaging algorithm.

Gel Shift Assays

To confirm the binding of PNAs to the target miR-210 RNA, 16% PAGE gel and Bolt electrophoresis system (Life Technologies) were used. Before loading, samples were prepared by mixing 0.5 μM miR-210 RNA and 0.5 μM or 1 μM PNA together and incubating them at 37°C overnight. Before loading into the gel, 2 μL of Bio-Rad nucleic acid stain was added and the gel was run at 120 V for 1.5 hr. SYBR Gold (Life Technologies) was used to visualize the miR-210 RNA.

Thermal Melting Analysis

All samples were prepared by mixing a stoichiometric amount of each strand (1 μM) in sodium phosphate buffer (10 mM sodium

phosphate, 100 mM NaCl, 0.1 mM EDTA, and 5 M urea) at pH 7. UV melting curves were collected using an Agilent Cary UV-Vis 300 spectrometer equipped with a thermoelectrically controlled multicell holder. UV melting spectra were collected by monitoring at 260 nm from 90°C to 20°C to 90°C, with a cooling/heating rate of 0.2°C/min. The cooling and heating curves were overlapped to confirm reversible denaturation. All recorded spectra were smoothed using a 20-point adjacent averaging algorithm, except RNA-$^{MP}\gamma P_{210}$ and DNA-$^{MP}\gamma P_{210}$, to avoid generating transition points. The first derivative of the melting curve was taken to determine the melting temperature of the duplex.

NP Formulation

PLGA NPs were loaded with 2 nmol/mg of PNAs and formulated using a double emulsion solvent evaporation method as previously described.[32] The encapsulant in water containing the PNAs was added dropwise to a polymer solution of 80 mg of 50:50 ester-terminated PLGA dissolved in 800 μL of dichloromethane (DCM), then ultrasonicated (3 times for 10 s) to form the first emulsion. This emulsion was added slowly dropwise to 1.6 mL of 5% aqueous polyvinyl alcohol, then ultrasonicated (3 times for 10 s) to form the second emulsion. Subsequently, this mixture was poured into 25 mL of 0.3% aqueous polyvinyl alcohol and stirred at room temperature for 3 hr. NPs were then washed with 25 mL of water three times and collected each time by centrifugation at 16,100 × *g* for 10 min at 4°C. Then NPs were resuspended in water containing trehalose, frozen at −80°C, and lyophilized. Particles were stored at −20°C following lyophilization.

Characterization of NPs

Release of PNAs from the NPs was analyzed by incubating 2-mg particles in 600 μL of PBS in a 37°C shaker, spinning down, and removing supernatant to measure absorbance at 260 nm at indicated time points using a Nanodrop 8000 (Thermo Fisher Scientific). A sample of particles from each batch was also analyzed using scanning electron microscopy. Samples were coated with 25-nm-thick palladium using a sputter coater. Images were analyzed using ImageJ software (NIH, Bethesda, MD), with >300 particles analyzed per batch to determine size distribution. Briefly, brightness, contrast, and threshold were adjusted to enhance particle outlines, and then ImageJ's "Analyze Particles" function was used to calculate the area of each particle. Hydrodynamic diameters of particles were analyzed with a Zetasizer Nano ZS (Malvern).

Real-Time qRT-PCR

Total RNA was extracted from cells with the mirVana Isolation kit (Applied Biosystems). cDNA was synthesized from total RNA using reverse transcription primers that were specific to miR-210 and the Taqman miRNA reverse transcription kit (Applied Biosystems). To assess miRNA, the cDNAs prepared from the specific reverse transcription reactions were used in PCRs containing Taqman Universal PCR Master Mix with no AmpErase UNG and premixed Taqman assays (Applied Biosystems). The Taqman assays for miRs only detect the mature miRs. Reactions were carried out in a 96-well optical reaction plate with optical caps (Agilent Technologies) in a Mx3000p Real-Time PCR Detection system spectrofluorometric thermal cycler (Agilent Technologies). Reactions proceeded with an initial 10-min incubation at 95°C, followed by 40 cycles of amplification: 95°C for 15 s and 60°C for 1 min. Fluorescence was measured in real time; the cycle threshold (C_t) values were calculated using the Mx3000p algorithm (Agilent Technologies). Comparative quantitation was performed by comparing the C_t value obtained from the amplification of a given target miRNA with that determined for the normalizer RNU6B. Relative miRNA abundance was calculated using the $-\Delta\Delta C_t$ method. Student's t test was used for statistical analysis.

Assays for PNA Delivery

Delivery of PNAs was tested in cell culture using HeLa cells cultured in DMEM with 10% fetal bovine serum (FBS). The cells were seeded in 8-chambered glass dishes and treated with 2 mg/mL NPs loaded with TAMRA-conjugated $^{MP}\gamma P_{210}$. After 24 hr, the cells were washed twice with PBS, stained with DAPI and carboxyfluorescein succinimidyl ester (CFSE)-488, and visualized using confocal microscopy. For assessment of in vivo delivery, HeLa tumor xenografts at a volume of 100 mm^3 (see below) were injected intratumorally with 6-mg NPs loaded with TAMRA-conjugated $^{MP}\gamma P_{210}$, and uptake of PNA was assayed after 24 hr. Ex vivo fluorescence imaging of resected tumors was performed on an IVIS Spectrum System (Caliper) using TAMRA filter sets with an exposure of 2 s and f-stop of 4. Tumors were then fixed in 4% paraformaldehyde (PFA) for 24 hr and then equilibrated in 15% sucrose for 18 hr and subsequently in 30% sucrose for 18 hr. Tumors were cryosectioned using a Leica cryostat CM3050s in 10 μm slices. Sections were first permeabilized using a 0.1% Triton-x solution for 15 min and washed twice with PBS. Then slides were stained with Phalloidin-488 for 10 min and washed 3 times with PBS before adding coverslips with VECTASHIELD mounting medium with DAPI. All confocal microscopy was performed with a Leica TCS SP5 and analyzed with Leica LAS X.

Mouse Tumor Xenografts

Athymic nude mice were purchased from Harlan. Mice were maintained at Yale University in accordance with the Yale Animal Resource Center and Institutional Animal Care and Use Committee guidelines. At 4 to 5 weeks of age, mice were injected subcutaneously with 5×10^6 HeLa cells suspended in DMEM media without FBS. Tumor take rate was >80%. When tumors reached 100-mm^3 geometric mean volumes, the mice were randomly assigned to treatment groups (n = 5 per group), and tumors were injected locally with 6 mg of either blank NPs or NPs containing the following PNAs: $^{MP}\gamma P_{mm}$, P_{210}, or $^{MP}\gamma P_{210}$. Prior to injection, NPs were suspended in PBS and administered intratumorally in a volume of 50 μL (120 mg/mL). Treatment was repeated after 10 days for a total of 2 doses of each batch of NPs. Tumor growth was assessed by external caliper measurements performed three times per week until the tumors reached 1,000 mm^3 in size or until 50 days, whichever came first. ANOVA was used for statistical analysis for each group relative to the blank group.

Histopathology

For histopathologic analysis, when tumors reached an approximate size of 100 mm^3, they were injected with 6 mg of either blank NPs or NPs containing the following PNAs: $^{MP}\gamma P_{mm}$, P_{210}, or $^{MP}\gamma P_{210}$, as above. On day 3 after treatment, the tumors were resected and fixed in 10% neutral-buffered formalin (NBF). Fixed tumor tissues were processed by Yale Pathology Tissue Services for H&E, Trichrome 6, caspase-3, and Ki67 staining. Image quantification used ImageJ version 1.47 (NIH) and the Color Deconvolution plugin (A.C. Ruifrok).

RNA and Protein Analyses from Tumor Samples

Mice were euthanized on day 3 after treatment with a single dose of 6-mg NPs, and HeLa cell xenograft tumors were excised and placed immediately in dissociation medium (10% DMEM + 1.2 mg/mL Dispase [STEMCELL Technologies] + 0.5 mg/mL Collagenase [Worthington Biochemical]). Tumors were then cut into small pieces using a sterile blade, suspended in 10 mL of dissociation medium per 1 g of tumor mass, and incubated for 1.5 hr at 37°C shaking at 190 rpm. The dissociated tumors were then centrifuged, washed with 1X PBS, centrifuged, and trypsinized for 3 min in 0.25% trypsin at room temperature. After the addition of 10% DMEM, cells were passed through a 70-μm filter, centrifuged, and incubated in 1X Red Blood Cell Lysis Buffer (Sigma) on ice for 10 min. After the addition of 1X PBS, cells were passed through a 40 μM filter, centrifuged, and resuspended in 0.5% BSA in 1X PBS. Mouse cells present in the tumor cell population were then removed using the Mouse Cell Depletion Kit (Miltenyi Biotec) according to the manufacturer's protocol, and purified human cell pellets were stored at −80°C. Tumor cell RNA was extracted from cells with the mirVana Isolation kit (Applied Biosystems) and analyzed as above by qRT-PCR.

Analysis of protein expression was conducted by western blotting, as previously described.[50] Briefly, human tumor cell pellets isolated as above were lysed in AZ lysis buffer (50 mmol/L Tris, 250 mmol/L NaCl, 1% Igepal, 0.1% SDS, 5 mmol/L EDTA, and 10 mmol/L $Na_2P_2O_7$) supplemented with Protease Inhibitor Cocktail (Roche) on ice for 20 min. Cellular debris was cleared by centrifugation, and lysate protein concentration was quantified using the DC Protein Assay (Bio-Rad). Lysate containing 80 μg of protein was subjected to SDS-PAGE in a Mini-PROTEAN TGX 4%–20% gradient gel (Bio-Rad) and then transferred to a nitrocellulose membrane. Proteins were detected with rabbit anti-Iscu1/2 primary antibody (Santa Cruz; sc-28860) and mouse anti-Vinculin primary antibody (Abcam; ab18058). Band intensities were quantified using ImageJ software, and Iscu1/2 expression was normalized to Vinculin expression.

SUPPLEMENTAL INFORMATION

Supplemental Information includes five figures and one table and can be found with this article online at https://doi.org/10.1016/j.omtn.2017.09.001.

AUTHOR CONTRIBUTIONS

Experiments were designed by A.G., P.M.G., and W.M.S. Experiments were performed and data were analyzed by A.G., E.Q., Y.L., R.B., S.E.S., E.S., W.-C.H., and D.E.B. Important reagents were prepared and provided by E.Q., R.B., and D.H.L. The manuscript was prepared by A.G., E.Q., P.M.G., and W.M.S.

CONFLICTS OF INTEREST

The authors declare no conflict of interest.

ACKNOWLEDGMENTS

We thank Denise Hegan, Yuhong Lu, Jennifer Czochor, Zhong Yun, Christopher Corso, and Hoon Kim for their technical assistance. This work was supported by grants from the NIH (R35CA197574, R01ES005775, and R01CA168733 to P.M.G.), the NIH/NIGMS Medical Scientist Training Program (T32GM007205 to E.Q.), the National Science Foundation (CHE-1609159 to D.H.L.), and the DSF Charitable Foundation (to D.H.L.).

REFERENCES

1. Alvarez-Garcia, I., and Miska, E.A. (2005). MicroRNA functions in animal development and human disease. Development *132*, 4653–4662.
2. Bushati, N., and Cohen, S.M. (2007). microRNA functions. Annu. Rev. Cell Dev. Biol. *23*, 175–205.
3. Su, Z., Chen, D., Li, Y., Zhang, E., Yu, Z., Chen, T., Jiang, Z., Ni, L., Yang, S., Gui, Y., et al. (2015). microRNA-184 functions as tumor suppressor in renal cell carcinoma. Exp. Ther. Med. *9*, 961–966.
4. Sun, B., Yang, M., Li, M., and Wang, F. (2015). The microRNA-217 functions as a tumor suppressor and is frequently downregulated in human osteosarcoma. Biomed. Pharmacother. *71*, 58–63.
5. Wang, B., Shen, Z.L., Jiang, K.W., Zhao, G., Wang, C.Y., Yan, Y.C., Yang, Y., Zhang, J.Z., Shen, C., Gao, Z.D., et al. (2015). MicroRNA-217 functions as a prognosis predictor and inhibits colorectal cancer cell proliferation and invasion via an AEG-1 dependent mechanism. BMC Cancer *15*, 437.
6. Wang, L.Q., Zhang, Y., Yan, H., Liu, K.J., and Zhang, S. (2015). MicroRNA-373 functions as an oncogene and targets YOD1 gene in cervical cancer. Biochem. Biophys. Res. Commun. *459*, 515–520.
7. Kulshreshtha, R., Ferracin, M., Wojcik, S.E., Garzon, R., Alder, H., Agosto-Perez, F.J., Davuluri, R., Liu, C.G., Croce, C.M., Negrini, M., et al. (2007). A microRNA signature of hypoxia. Mol. Cell. Biol. *27*, 1859–1867.
8. Rupaimoole, R., Ivan, C., Yang, D., Gharpure, K.M., Wu, S.Y., Pecot, C.V., Previs, R.A., Nagaraja, A.S., Armaiz-Pena, G.N., McGuire, M., et al. (2016). Hypoxia-upregulated microRNA-630 targets Dicer, leading to increased tumor progression. Oncogene *35*, 4312–4320.
9. Crosby, M.E., Kulshreshtha, R., Ivan, M., and Glazer, P.M. (2009). MicroRNA regulation of DNA repair gene expression in hypoxic stress. Cancer Res. *69*, 1221–1229.
10. Ho, A.S., Huang, X., Cao, H., Christman-Skieller, C., Bennewith, K., Le, Q.T., and Koong, A.C. (2010). Circulating miR-210 as a novel hypoxia marker in pancreatic cancer. Transl. Oncol. *3*, 109–113.
11. Grosso, S., Doyen, J., Parks, S.K., Bertero, T., Paye, A., Cardinaud, B., Gounon, P., Lacas-Gervais, S., Noël, A., Pouysségur, J., et al. (2013). MiR-210 promotes a hypoxic phenotype and increases radioresistance in human lung cancer cell lines. Cell Death Dis. *4*, e544.
12. Qin, Q., Furong, W., and Baosheng, L. (2014). Multiple functions of hypoxia-regulated miR-210 in cancer. J. Exp. Clin. Cancer. Res. *33*, 50.
13. Lawrie, C.H., Gal, S., Dunlop, H.M., Pushkaran, B., Liggins, A.P., Pulford, K., Banham, A.H., Pezzella, F., Boultwood, J., Wainscoat, J.S., et al. (2008). Detection of elevated levels of tumour-associated microRNAs in serum of patients with diffuse large B-cell lymphoma. Br. J. Haematol. *141*, 672–675.
14. Zhao, A., Li, G., Péoc'h, M., Genin, C., and Gigante, M. (2013). Serum miR-210 as a novel biomarker for molecular diagnosis of clear cell renal cell carcinoma. Exp. Mol. Pathol. *94*, 115–120.

15. Favaro, E., Ramachandran, A., McCormick, R., Gee, H., Blancher, C., Crosby, M., Devlin, C., Blick, C., Buffa, F., Li, J.L., et al. (2010). MicroRNA-210 regulates mitochondrial free radical response to hypoxia and krebs cycle in cancer cells by targeting iron sulfur cluster protein ISCU. PLoS ONE *5*, e10345.

16. Qin, L., Chen, Y., Niu, Y., Chen, W., Wang, Q., Xiao, S., Li, A., Xie, Y., Li, J., Zhao, X., et al. (2010). A deep investigation into the adipogenesis mechanism: profile of microRNAs regulating adipogenesis by modulating the canonical Wnt/beta-catenin signaling pathway. BMC Genomics *11*, 320.

17. Zuo, J., Wen, M., Lei, M., Peng, X., Yang, X., and Liu, Z. (2015). MiR-210 links hypoxia with cell proliferation regulation in human laryngocarcinoma cancer. J. Cell. Biochem. *116*, 1039–1049.

18. Kasinski, A.L., and Slack, F.J. (2011). Epigenetics and genetics. MicroRNAs en route to the clinic: progress in validating and targeting microRNAs for cancer therapy. Nat. Rev. Cancer *11*, 849–864.

19. Flemming, A. (2014). Cancer: new delivery platform targets antimirs to tumours. Nat. Rev. Drug Discov. *13*, 888.

20. Catuogno, S., Rienzo, A., Di Vito, A., Esposito, C.L., and de Franciscis, V. (2015). Selective delivery of therapeutic single strand antimiRs by aptamer-based conjugates. J. Control Release *210*, 147–159.

21. Cheng, C.J., Bahal, R., Babar, I.A., Pincus, Z., Barrera, F., Liu, C., Svoronos, A., Braddock, D.T., Glazer, P.M., Engelman, D.M., et al. (2015). MicroRNA silencing for cancer therapy targeted to the tumour microenvironment. Nature *518*, 107–110.

22. Elmén, J., Lindow, M., Schütz, S., Lawrence, M., Petri, A., Obad, S., Lindholm, M., Hedtjärn, M., Hansen, H.F., Berger, U., et al. (2008). LNA-mediated microRNA silencing in non-human primates. Nature *452*, 896–899.

23. Elmén, J., Lindow, M., Silahtaroglu, A., Bak, M., Christensen, M., Lind-Thomsen, A., Hedtjärn, M., Hansen, J.B., Hansen, H.F., Straarup, E.M., et al. (2008). Antagonism of microRNA-122 in mice by systemically administered LNA-antimiR leads to up-regulation of a large set of predicted target mRNAs in the liver. Nucleic Acids Res. *36*, 1153–1162.

24. Manicardi, A., Fabbri, E., Tedeschi, T., Sforza, S., Bianchi, N., Brognara, E., Gambari, R., Marchelli, R., and Corradini, R. (2012). Cellular uptakes, biostabilities and anti-miR-210 activities of chiral arginine-PNAs in leukaemic K562 cells. ChemBioChem *13*, 1327–1337.

25. Fabani, M.M., and Gait, M.J. (2008). miR-122 targeting with LNA/2′-O-methyl oligonucleotide mixmers, peptide nucleic acids (PNA), and PNA-peptide conjugates. RNA *14*, 336–346.

26. Fabani, M.M., Abreu-Goodger, C., Williams, D., Lyons, P.A., Torres, A.G., Smith, K.G., Enright, A.J., Gait, M.J., and Vigorito, E. (2010). Efficient inhibition of miR-155 function in vivo by peptide nucleic acids. Nucleic Acids Res. *38*, 4466–4475.

27. Fabbri, E., Manicardi, A., Tedeschi, T., Sforza, S., Bianchi, N., Brognara, E., Finotti, A., Breveglieri, G., Borgatti, M., Corradini, R., et al. (2011). Modulation of the biological activity of microRNA-210 with peptide nucleic acids (PNAs). ChemMedChem *6*, 2192–2202.

28. Nielsen, P.E., Egholm, M., Berg, R.H., and Buchardt, O. (1991). Sequence-selective recognition of DNA by strand displacement with a thymine-substituted polyamide. Science *254*, 1497–1500.

29. Cheng, C.J., and Saltzman, W.M. (2012). Polymer nanoparticle-mediated delivery of microRNA inhibition and alternative splicing. Mol. Pharm. *9*, 1481–1488.

30. Yeh, J.I., Shivachev, B., Rapireddy, S., Crawford, M.J., Gil, R.R., Du, S., Madrid, M., and Ly, D.H. (2010). Crystal structure of chiral gammaPNA with complementary DNA strand: insights into the stability and specificity of recognition and conformational preorganization. J. Am. Chem. Soc. *132*, 10717–10727.

31. Bahal, R., Sahu, B., Rapireddy, S., Lee, C.-M., and Ly, D.H. (2012). Sequence-unrestricted, Watson-Crick recognition of double helical B-DNA by (R)-miniPEG-γPNAs. ChemBioChem *13*, 56–60.

32. Bahal, R., McNeer, N.A., Ly, D.H., Saltzman, W.M., and Glazer, P.M. (2013). Nanoparticle for delivery of antisense γPNA oligomers targeting CCR5. Artif. DNA PNA XNA *4*, 49–57.

33. Bahal, R., Quijano, E., McNeer, N.A., Liu, Y., Bhunia, D.C., Lopez-Giraldez, F., Fields, R.J., Saltzman, W.M., Ly, D.H., and Glazer, P.M. (2014). Single-stranded γPNAs for in vivo site-specific genome editing via Watson-Crick recognition. Curr. Gene Ther. *14*, 331–342.

34. Manna, A., Rapireddy, S., Bahal, R., and Ly, D.H. (2014). MiniPEG-γPNA. Methods Mol. Biol. *1050*, 1–12.

35. Dragulescu-Andrasi, A., Rapireddy, S., Frezza, B.M., Gayathri, C., Gil, R.R., and Ly, D.H. (2006). A simple gamma-backbone modification preorganizes peptide nucleic acid into a helical structure. J. Am. Chem. Soc. *128*, 10258–10267.

36. Gupta, A., Bahal, R., Gupta, M., Glazer, P.M., and Saltzman, W.M. (2016). Nanotechnology for delivery of peptide nucleic acids (PNAs). J. Control Release *240*, 302–311.

37. Bahal, R., Ali McNeer, N., Quijano, E., Liu, Y., Sulkowski, P., Turchick, A., Lu, Y.C., Bhunia, D.C., Manna, A., Greiner, D.L., et al. (2016). In vivo correction of anaemia in β-thalassemic mice by γPNA-mediated gene editing with nanoparticle delivery. Nat. Commun. *7*, 13304.

38. Babar, I.A., Cheng, C.J., Booth, C.J., Liang, X., Weidhaas, J.B., Saltzman, W.M., and Slack, F.J. (2012). Nanoparticle-based therapy in an in vivo microRNA-155 (miR-155)-dependent mouse model of lymphoma. Proc. Natl. Acad. Sci. USA *109*, E1695–E1704.

39. Chan, S.Y., Zhang, Y.Y., Hemann, C., Mahoney, C.E., Zweier, J.L., and Loscalzo, J. (2009). MicroRNA-210 controls mitochondrial metabolism during hypoxia by repressing the iron-sulfur cluster assembly proteins ISCU1/2. Cell Metab. *10*, 273–284.

40. He, G., Rapireddy, S., Bahal, R., Sahu, B., and Ly, D.H. (2009). Strand invasion of extended, mixed-sequence B-DNA by gammaPNAs. J. Am. Chem. Soc. *131*, 12088–12090.

41. Rapireddy, S., He, G., Roy, S., Armitage, B.A., and Ly, D.H. (2007). Strand invasion of mixed-sequence B-DNA by acridine-linked, gamma-peptide nucleic acid (gamma-PNA). J. Am. Chem. Soc. *129*, 15596–15600.

42. Rapireddy, S., Bahal, R., and Ly, D.H. (2011). Strand invasion of mixed-sequence, double-helical B-DNA by γ-peptide nucleic acids containing G-clamp nucleobases under physiological conditions. Biochemistry *50*, 3913–3918.

43. Gee, H.E., Camps, C., Buffa, F.M., Patiar, S., Winter, S.C., Betts, G., Homer, J., Corbridge, R., Cox, G., West, C.M., et al. (2010). hsa-mir-210 is a marker of tumor hypoxia and a prognostic factor in head and neck cancer. Cancer *116*, 2148–2158.

44. Camps, C., Buffa, F.M., Colella, S., Moore, J., Sotiriou, C., Sheldon, H., Harris, A.L., Gleadle, J.M., and Ragoussis, J. (2008). hsa-miR-210 Is induced by hypoxia and is an independent prognostic factor in breast cancer. Clin. Cancer Res. *14*, 1340–1348.

45. Yang, W., Sun, T., Cao, J., Liu, F., Tian, Y., and Zhu, W. (2012). Downregulation of miR-210 expression inhibits proliferation, induces apoptosis and enhances radiosensitivity in hypoxic human hepatoma cells in vitro. Exp. Cell Res. *318*, 944–954.

46. Yang, W., Wei, J., Sun, T., and Liu, F. (2013). Effects of knockdown of miR-210 in combination with ionizing radiation on human hepatoma xenograft in nude mice. Radiat. Oncol. *8*, 102.

47. Huang, X., Ding, L., Bennewith, K.L., Tong, R.T., Welford, S.M., Ang, K.K., Story, M., Le, Q.T., and Giaccia, A.J. (2009). Hypoxia-inducible mir-210 regulates normoxic gene expression involved in tumor initiation. Mol. Cell *35*, 856–867.

48. Giannakakis, A., Sandaltzopoulos, R., Greshock, J., Liang, S., Huang, J., Hasegawa, K., Li, C., O'Brien-Jenkins, A., Katsaros, D., Weber, B.L., et al. (2008). miR-210 links hypoxia with cell cycle regulation and is deleted in human epithelial ovarian cancer. Cancer Biol. Ther. *7*, 255–264.

49. Sahu, B., Sacui, I., Rapireddy, S., Zanotti, K.J., Bahal, R., Armitage, B.A., and Ly, D.H. (2011). Synthesis and characterization of conformationally preorganized, (R)-diethylene glycol-containing γ-peptide nucleic acids with superior hybridization properties and water solubility. J. Org. Chem. *76*, 5614–5627.

50. Scanlon, S.E., and Glazer, P.M. (2014). Hypoxic stress facilitates acute activation and chronic downregulation of fanconi anemia proteins. Mol. Cancer Res. *12*, 1016–1028.